

Rayleigh-Gauss-Newton optimization with enhanced sampling for variational Monte Carlo

Robert J. Webber and Michael Lindsey

Courant Institute of Mathematical Sciences, New York University, New York 10012, USA

Variational Monte Carlo (VMC) is an approach for computing ground-state wavefunctions that has recently become more powerful due to the introduction of neural network-based wavefunction parametrizations. However, efficiently training neural wavefunctions to converge to an energy minimum remains a difficult problem. In this work, we analyze optimization and sampling methods used in VMC and introduce alterations to improve their performance. First, based on theoretical convergence analysis in a noiseless setting, we motivate a new optimizer that we call the Rayleigh-Gauss-Newton method, which can improve upon gradient descent and natural gradient descent to achieve superlinear convergence with little added computational cost. Second, in order to realize this favorable comparison in the presence of stochastic noise, we analyze the effect of sampling error on VMC parameter updates and experimentally demonstrate that it can be reduced by the parallel tempering method. In particular, we demonstrate that RGN can be made robust to energy spikes that occur when new regions of configuration space become available to the sampler over the course of optimization. Finally, putting theory into practice, we apply our enhanced optimization and sampling methods to the transverse-field Ising and XXZ models on large lattices, yielding ground-state energy estimates with remarkably high accuracy after just 200–500 parameter updates.

I. INTRODUCTION

Computing the ground-state wavefunction of a many-body Hamiltonian operator is a demanding task, requiring the solution of an eigenvalue problem whose cost grows exponentially with system size using traditional numerical approaches. Variational Monte Carlo (VMC, [1, 2]) is an approach that avoids this curse of dimensionality by using stochastic optimization to find the best wavefunction within a tractable function class. VMC has recently seen rapid and encouraging development due to the incorporation of insights from the machine learning community. In 2017, Carleo and Troyer [3] applied VMC with a two-layer neural network ansatz to accurately represent the ground-state wavefunction of quantum spin systems with as many as 100 spins. Since then, there has been major progress in extending neural network-based VMC to the setting of electronic structure, including the development of the neural network backflow ansatz for second-quantized lattice problems [4], as well as of FermiNet [5] and PauliNet [6] for quantum chemistry problems in first quantization. These new approaches have been extended to systems as large as bicyclobutane (C_4H_6), which has 30 interacting electrons [5, 7].

VMC is highly flexible, since it extends without significant modification to systems of arbitrary spatial dimension. However, the price paid for this flexibility is a difficult optimization problem that relies on Monte Carlo sampling. Efficiently solving this optimization problem has proven challenging. Recent works [4, 6–10] raise concerns about the speed and stability of wavefunction training and report that VMC can suffer from long training times [5, 7], lose stability [10], or converge to unreasonable solutions [11]. Thus there is motivation for the development of faster and more stable optimization and sampling solutions.

Our goal is to apply numerical and probabilistic analysis to evaluate and improve upon the optimization and

sampling strategies in VMC. To this end, we first provide a unified perspective on several major VMC optimizers, namely gradient descent, quantum natural gradient descent (also known as stochastic reconfiguration), and the linear method. Reviewing these methods in a unified way clarifies a path toward improvement. Specifically, we introduce a new *Rayleigh-Gauss-Newton* (RGN) method and prove RGN achieves superlinear convergence as the wavefunction approaches the ground state.

Next we analyze the stochastic sampling used in VMC. We establish a quantitative extension of the zero-variance principle [1, 2] of VMC that we call the vanishing-variance principle. The vanishing-variance principle guarantees that stochastic noise in energy and energy gradient estimates converges to zero as the wavefunction nears an eigenstate. However, despite the vanishing variance, the gradients themselves converge to zero when approaching an eigenstate, so the relative accuracy of gradient estimates is *not* guaranteed.

Due to the presence of gradient error, the quality of VMC sampling plays a major role in determining convergence. Specifically, as the wavefunction changes during optimization, sometimes new regions of configuration space suddenly become available to the sampler for exploration. These events may result in spikes in the energy estimate. Using standard MCMC samplers as in [3], the wavefunction is slow to recover from the energy spikes; however, by using the parallel tempering method [12] RGN can be made robust to the energy spikes, without comprising its desirable convergence properties.

Lastly, we obtain highly accurate variational estimates for the ground-state energies of transverse-field Ising and XXZ models with as many as 400 spins. Compared to past benchmark results obtained using natural gradient descent [3], we obtain the same or higher accuracy in fewer iterations by using the Rayleigh-Gauss-Newton method along with parallel tempering. Since RGN is only slightly more expensive than natural gradient descent (by

less than a factor of two, empirically), we conclude that RGN improves the overall efficiency of VMC.

The rest of the paper is organized as follows. Section II gives an overview of variational Monte Carlo, Section III analyzes optimization methods, Section IV analyzes sampling methods, Section V presents numerical experiments, and Section VI concludes.

Throughout the paper, $\Re z$ denotes the real part of a complex number z . \mathbf{v}^T , $\bar{\mathbf{v}}$, and \mathbf{v}^* denote the transpose, complex conjugate, and conjugate transpose of a vector \mathbf{v} , and similar conventions are adopted for matrices. We use single bars $|\cdot|$ for the Euclidean norm of a scalar, vector, or matrix and $\|\cdot\|_2$ for the spectral norm of a matrix. Lastly, we consider a finite- or infinite-dimensional Hilbert space of unnormalized wavefunctions ψ and use $\langle \cdot, \cdot \rangle$ and $\|\cdot\|$ to denote the associated inner product and norm.

II. OVERVIEW OF VMC

The main goal of variational Monte Carlo (VMC) is the identification of the ground-state energy and wavefunction of the Hamiltonian operator \mathcal{H} for a quantum many-body system. We denote the ground-state energy and wavefunction using λ_0 and ψ_0 , respectively. In addition to solving the eigenvalue equation $\mathcal{H}\psi_0 = \lambda_0\psi_0$, these admit a variational characterization in terms of the energy functional

$$\mathcal{E}[\psi] = \frac{\langle \psi, \mathcal{H}\psi \rangle}{\langle \psi, \psi \rangle}.$$

The ground-state energy λ_0 is the minimum value of \mathcal{E} , and the ground-state wavefunction ψ_0 is the minimizer of \mathcal{E} , which we assume to be unique up to an arbitrary multiplicative constant.

Identifying λ_0 and ψ_0 can become difficult when the Hilbert space associated with \mathcal{H} is high-dimensional or infinite-dimensional. For example, in the Heisenberg model for spin-1/2 particles on a graph [13], \mathcal{H} is the operator

$$\mathcal{H} = \sum_{i \sim j} J_x \sigma_i^x \sigma_j^x + J_y \sigma_i^y \sigma_j^y + J_z \sigma_i^z \sigma_j^z + h \sum_i \sigma_i^x,$$

where σ_i^x , σ_i^y , and σ_i^z are Pauli operators for the i -th spin, $i \sim j$ signifies that i and j are neighboring spins, and J_x , J_y , J_z , and h are real-valued parameters. In the case, e.g., of a 10×10 square lattice, the ground-state wavefunction can be viewed as a vector of length 2^{100} , which is far too large to store in memory, much less calculate with any conventional eigensolver, direct or iterative.

VMC must approximate this high-dimensional eigenvector using a tractable parametrization $\psi = \psi_{\theta}$, where θ is a vector of real- or complex-valued parameters. VMC uses an iterative approach for updating the θ parameters, with the goal of minimizing the energy within the parametric class. VMC iterates over the following three steps.

1. Draw random samples from the wavefunction density $\rho_{\theta} = |\psi_{\theta}|^2 / \langle \psi_{\theta}, \psi_{\theta} \rangle$.
2. Use the random samples to estimate the energy $\mathcal{E}[\psi_{\theta}]$, the energy gradient $\nabla_{\theta} \mathcal{E}[\psi_{\theta}]$, and possibly other quantities needed for the optimization.
3. Update the θ parameters to reduce the energy.

In VMC, we ideally find that the estimated energies fall quickly in the first iterations and decrease more slowly at subsequent iterations, yielding increasingly accurate estimates of λ_0 , as shown in Figure 1.

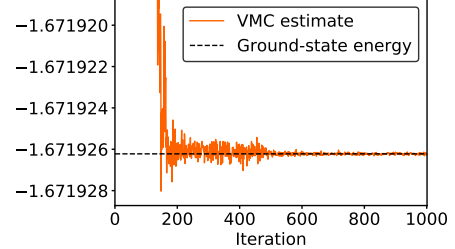


FIG. 1. VMC ground-state energy estimates for a 200×1 Ising model with a transverse magnetic field ($h = 1.5$). Computational details are provided in Section V.

Additionally, as seen in Figure 1, there is a *vanishing-variance principle* by which the energy estimator's variance converges to zero as the wavefunction approaches the ground state of \mathcal{H} (see Proposition 3). Because of this principle, reductions in the energy mean and reductions in the energy variance both indicate that the wavefunction is approaching the ground state. The vanishing-variance principle is essential in applications, since it enables VMC to provide accurate energy estimates even though the stochastic noise at the early stages of the optimization would appear to render such high accuracy impossible.

III. OPTIMIZATION APPROACHES

In this section, we obtain formulas for the energy gradient and Hessian, use these formulas to motivate optimization methods for VMC, and lastly derive theoretical convergence rates for VMC optimizers. Throughout the section, we assume that optimization methods are applied exactly without any stochastic sampling.

III.1. The energy gradient and Hessian

To begin, we derive formulas for the energy gradient and Hessian with respect to the parameters. By adopting the convention of intermediate normalization [14], we obtain compact expressions for these quantities that differ from some presentations, e.g., [1, ch. 9].

We fix a vector of parameters θ and then consider a small parameter update $\theta + \delta$. The resulting wavefunc-

tion, after intermediate normalization, is written

$$\hat{\psi}_{\theta+\delta} = \frac{\langle \psi_{\theta}, \psi_{\theta} \rangle}{\langle \psi_{\theta}, \psi_{\theta+\delta} \rangle} \psi_{\theta+\delta}.$$

This intermediate-normalized wavefunction is a scalar multiple of the unnormalized wavefunction $\psi_{\theta+\delta}$ and hence has the same energy. However, $\hat{\psi}_{\theta+\delta}$ has been rescaled to fix the inner product with ψ_{θ} .

We assume that $\delta \mapsto \hat{\psi}_{\theta+\delta}$ is a locally analytic function of real or complex parameters and consider the second-order Taylor series expansion

$$\hat{\psi}_{\theta+\delta} = \hat{\psi} + \sum_i \delta_i \hat{\psi}_i + \frac{1}{2} \sum_{ij} \delta_i \delta_j \hat{\psi}_{ij} + \mathcal{O}(|\delta|^3), \quad (1)$$

where $\hat{\psi}$, $\hat{\psi}_i$, and $\hat{\psi}_{ij}$ denote the normalized wavefunction and its partial derivatives

$$\hat{\psi} = \hat{\psi}_{\theta}, \quad \hat{\psi}_i = \partial_{\theta_i} \hat{\psi}_{\theta}, \quad \hat{\psi}_{ij} = \partial_{\theta_i} \partial_{\theta_j} \hat{\psi}_{\theta}.$$

Manipulating (1), we then decompose the energy difference $\mathcal{E}[\hat{\psi}_{\theta+\delta}] - \mathcal{E}[\hat{\psi}_{\theta}]$ into the sum of gradient and Hessian terms

$$\underbrace{\mathcal{E}[\hat{\psi}_{\theta+\delta}] - \mathcal{E}[\hat{\psi}_{\theta}]}_{\text{energy difference}} = \underbrace{\delta^* \mathbf{g} + \mathbf{g}^* \delta}_{\text{gradient terms}} + \underbrace{\delta^* \mathbf{H} \delta + \Re(\delta^T \mathbf{J} \delta)}_{\text{Hessian terms}} + \mathcal{O}(|\delta|^3).$$

These gradient and Hessian terms are given explicitly by

$$\mathbf{g}_i = \frac{\langle \hat{\psi}_i, \hat{\mathcal{H}} \hat{\psi} \rangle}{\langle \hat{\psi}, \hat{\psi} \rangle}, \quad \mathbf{H}_{ij} = \frac{\langle \hat{\psi}_i, \hat{\mathcal{H}} \hat{\psi}_j \rangle}{\langle \hat{\psi}, \hat{\psi} \rangle}, \quad (2)$$

$$\mathbf{J}_{ij} = \frac{\langle \hat{\psi}_{ij}, \hat{\mathcal{H}} \hat{\psi} \rangle}{\langle \hat{\psi}, \hat{\psi} \rangle}, \quad (3)$$

where $\hat{\mathcal{H}} = \mathcal{H} - \mathcal{E}[\hat{\psi}]$ is an energy-shifted version of the operator \mathcal{H} .

Equations (2) and (3) offer transparent formulas for the energy gradient and Hessian. In the case of real-valued parameters, the energy gradient is $2\mathbf{g}$, and the energy Hessian is $2\mathbf{H} + 2\mathbf{J}$. In the case of complex-valued parameters (such as in the setting of [3]), the Wirtinger gradient [15, 16] of the energy is $(\frac{\mathbf{g}}{\mathbf{g}})$, and the Wirtinger Hessian is $(\frac{\mathbf{H} \mathbf{J}}{\mathbf{J} \mathbf{H}})$. For simplicity, we call \mathbf{g} the energy gradient throughout this work.

The structure of the Hessian simplifies near the ground state, since $\mathbf{J} \rightarrow 0$ as the wavefunction approaches any eigenstate of \mathcal{H} .

Proposition 1. *The matrix \mathbf{J} is bounded by*

$$|\mathbf{J}_{ij}| \leq \frac{\|\hat{\psi}_{ij}\|}{\|\hat{\psi}\|} \min_{\lambda \in \mathbb{R}} \frac{\|(\mathcal{H} - \lambda) \hat{\psi}\|}{\|\hat{\psi}\|}$$

Therefore, $\mathbf{J} \rightarrow 0$ as $\min_{\lambda \in \mathbb{R}} \|(\mathcal{H} - \lambda) \hat{\psi}\| / \|\hat{\psi}\| \rightarrow 0$, assuming uniformly bounded $\|\hat{\psi}_{ij}\| / \|\hat{\psi}\|$ terms.

Proof. Apply the Cauchy-Schwartz inequality to (3), and use the fact that $\|\hat{\mathcal{H}} \hat{\psi}\| = \min_{\lambda \in \mathbb{R}} \|(\mathcal{H} - \lambda) \hat{\psi}\|$. \square

As the wavefunction approaches an eigenstate, Proposition 1 reveals that the Hessian or Wirtinger Hessian takes a simple structure, depending only on first derivatives of the wavefunction. To our knowledge this fact has not been previously identified. An important implication, to be spelled out below in Subsection III.4, is that first derivatives suffice to achieve superlinear convergence in VMC optimization, under the assumption that the true ground state lies within our parametric class.

III.2. Gradient descent methods

The main idea in gradient descent methods is to first approximate the energy using

$$\mathcal{E}_{\text{linear}}[\hat{\psi}_{\theta+\delta}] - \mathcal{E}[\hat{\psi}_{\theta}] = \delta^* \mathbf{g} + \mathbf{g}^* \delta \quad (4)$$

and then choose δ to minimize (4), plus an penalization term that keeps the update small. The penalization term may take the form

$$\frac{|\delta|^2}{\epsilon} \quad \text{or} \quad \frac{\angle(\hat{\psi}_{\theta}, \hat{\psi}_{\theta+\delta})^2}{\epsilon},$$

where $\epsilon > 0$ is a tunable parameter. In the first case, we are restricting the Euclidean norm $|\delta|$ and the resulting method is standard gradient descent. In the second case, we are restricting the angle between wavefunctions

$$\angle(\hat{\psi}_{\theta}, \hat{\psi}_{\theta+\delta}) = \arccos \frac{|\langle \hat{\psi}_{\theta}, \hat{\psi}_{\theta+\delta} \rangle|}{\|\hat{\psi}_{\theta}\| \|\hat{\psi}_{\theta+\delta}\|}.$$

This leads to a method called ‘stochastic reconfiguration’ or ‘quantum natural gradient descent’ [2], which has been used extensively to optimize traditional [17, 18] and more recent [3, 5] VMC wavefunction ansatzes.

In a high-dimensional or infinite-dimensional Hilbert space, the angle $\angle(\hat{\psi}_{\theta}, \hat{\psi}_{\theta+\delta})$ cannot be computed exactly, so natural gradient descent takes advantage of the Taylor series expansion

$$\angle(\hat{\psi}_{\theta}, \hat{\psi}_{\theta+\delta})^2 = \delta^* \mathbf{S} \delta + \mathcal{O}(|\delta|^3), \quad (5)$$

where

$$\mathbf{S}_{ij} = \frac{\langle \hat{\psi}_i, \hat{\psi}_j \rangle}{\langle \hat{\psi}, \hat{\psi} \rangle}$$

is a positive semidefinite matrix known as the Fubini-Study metric or quantum information metric [19]. Natural gradient descent uses the penalization term

$$\frac{\delta^* (\mathbf{S} + \eta \mathbf{I}) \delta}{\epsilon},$$

where $\eta > 0$ is a parameter that is necessary due to the neglected higher-order terms in the Taylor series expansion (5).

To make the preceding discussion precise, we formalize gradient descent (GD) methods as follows.

Algorithm 1 (GD methods). *Choose δ to solve*

$$\min_{\delta} \left[\delta^* \mathbf{g} + \mathbf{g}^* \delta + \frac{\delta^* \mathbf{R} \delta}{\epsilon} \right],$$

where $\mathbf{R} = \mathbf{I}$ in GD and $\mathbf{R} = \mathbf{S} + \eta \mathbf{I}$ in natural GD. Equivalently, set

$$\delta = -\epsilon \mathbf{R}^{-1} \mathbf{g}.$$

In addition to GD and natural GD, alternative gradient descent methods such as Adam [20] and AMSGrad [21] have recently gained traction in the VMC community [5, 22–24]. These ‘momentum-based’ methods form updates by combining the energy gradient at the current iteration and past iterations. While such strategies are potentially promising, recent tests [5, 25] reveal that natural GD still outperforms momentum-based methods on several challenging VMC test problems. Therefore, we focus on GD and natural GD, leaving analysis of other gradient descent methods for future work.

III.3. Rayleigh-Gauss-Newton method

Whereas gradient descent methods are based on a linear approximation of the energy, we now introduce a method—which we call the Rayleigh-Gauss-Newton (RGN) method—based on the following quadratic energy approximation:

$$\mathcal{E}_{\text{quad}}[\hat{\psi}_{\theta+\delta}] - \mathcal{E}[\hat{\psi}_{\theta}] = \delta^* \mathbf{g} + \mathbf{g}^* \delta + \delta^* \mathbf{H} \delta. \quad (6)$$

Here, $\delta^* \mathbf{g}$ and $\mathbf{g}^* \delta$ are the exact gradient terms, while $\delta^* \mathbf{H} \delta$ is just one of the Hessian terms. There is a strong practical motivation for ignoring the other Hessian term $\Re(\delta^T \mathbf{J} \delta)$, since evaluating this term would require taking second derivatives of the wavefunction with respect to all pairs of parameters, which becomes burdensome as the number of parameters grows large.

In the RGN method, we minimize the quadratic objective function (6) plus a ‘natural’ penalization term, as described below.

Algorithm 2 (RGN method). *Choose δ to solve*

$$\min_{\delta} \left[\delta^* \mathbf{g} + \mathbf{g}^* \delta + \delta^* \mathbf{H} \delta + \frac{\delta^* \mathbf{R} \delta}{\epsilon} \right],$$

where $\mathbf{R} = \mathbf{S} + \eta \mathbf{I}$. Equivalently, set

$$\delta = -(\mathbf{H} + \epsilon^{-1} \mathbf{R})^{-1} \mathbf{g}.$$

To our knowledge, the RGN method has not appeared before in the literature. However, it is closely connected to the classical Gauss-Newton method for nonlinear least squares problems [26], which can be viewed as deriving from a similar Hessian splitting. Also, RGN is related to several VMC optimization methods, including the linear method for energy minimization [2] and a Gauss-Newton-like method for variance minimization [27]. In all these

previous approaches, the main idea is to minimize a loss functional $\mathcal{L}[\hat{\psi}_{\theta}]$ by first linearizing the function $\hat{\psi}_{\theta}$. The linearization of $\hat{\psi}_{\theta}$ yields an approximate loss functional

$$\mathcal{L}[\hat{\psi}_{\theta+\delta}] \approx \mathcal{L}[\hat{\psi} + \sum_i \delta_i \hat{\psi}_i].$$

The parameter update δ is then chosen to minimize $\mathcal{L}[\hat{\psi} + \sum_i \delta_i \hat{\psi}_i]$, plus a penalization term that keeps the update small.

For example, in the linear method for VMC, one first linearizes the intermediate-normalized wavefunction $\hat{\psi}_{\theta+\delta}$ to yield an approximate energy functional

$$\mathcal{E} \left[\hat{\psi} + \sum_i \delta_i \hat{\psi}_i \right] = \mathcal{E} \left[\hat{\psi} \right] + \frac{\delta^* \mathbf{g} + \mathbf{g}^* \delta + \delta^* \mathbf{H} \delta}{1 + \delta^* \mathbf{S} \delta} \quad (7)$$

and then chooses δ to minimize (7), plus an additional penalization term. Minimization of (7) is equivalent to solving the generalized eigenvalue problem

$$\begin{pmatrix} 0 & \mathbf{g}^* \\ \mathbf{g} & \mathbf{H} \end{pmatrix} \begin{pmatrix} 1 \\ \delta \end{pmatrix} = \lambda \begin{pmatrix} 1 & \mathbf{0} \\ \mathbf{0} & \mathbf{S} \end{pmatrix} \begin{pmatrix} 1 \\ \delta \end{pmatrix}$$

for the lowest eigenvalue-eigenvector pair [1, 2]. As a penalization term, the matrix \mathbf{H} is padded with a diagonal matrix $\epsilon^{-1} \mathbf{I}$, which is similar to the penalization term used in GD. The linear method has been observed to yield fast asymptotic convergence in VMC applications with small parameter sets. However, extending the linear method to larger parameter sets is an ongoing challenge [22, 28].

Motivated by the linear method’s potential for fast asymptotic convergence, we introduce RGN as an updated strategy with improved stability properties. RGN differs from the linear method in three ways, as detailed below.

First, instead of approximating the energy using the formula (7), RGN uses a quadratic approximation

$$\mathcal{E}_{\text{quad}}[\hat{\psi}_{\theta+\delta}] - \mathcal{E}[\hat{\psi}_{\theta}] = \delta^* \mathbf{g} + \mathbf{g}^* \delta + \delta^* \mathbf{H} \delta.$$

This quadratic approximation agrees with (7) up to $\mathcal{O}(|\delta|^3)$ terms, but it leads to parameter updates that are more robust in the presence of VMC sampling error.

Second, RGN uses a ‘natural’ penalization term $\epsilon^{-1} \delta^* (\mathbf{S} + \eta \mathbf{I}) \delta$, which is different from the penalization term used in the linear method. Because of the penalization, the linear method converges as $\epsilon \rightarrow 0$ to give standard GD updates. In contrast, RGN converges as $\epsilon \rightarrow 0$ to give natural GD updates, which are more efficient than standard GD updates when optimizing many VMC wavefunction ansatzes [5, 25].

Finally, RGN only requires the solution of a linear system instead of a generalized eigenvalue problem. Although the parametrizations considered in our numerical experiments below are small enough so that neither of these linear algebra routines imposes a computational bottleneck, the distinction may become quite important for large parameter sets. For example, matrix inversion admits efficient low-rank updates, which may be used

as in [5] to exploit memory of previous iterations in the stochastic estimation of the relevant matrices. Moreover, there is improved potential for a matrix-free implementation of RGN for very large parametrizations. Indeed, [28] introduced a matrix-free approach for solving the linear system in stochastic reconfiguration, but a similar scheme for the generalized eigenvalue problem has not achieved the same success [29].

III.4. Convergence rate analysis

GD, natural GD, and RGN can all be presented in the standardized form

$$\mathbf{P}^i(\boldsymbol{\theta}^{i+1} - \boldsymbol{\theta}^i) = -\mathbf{g}(\boldsymbol{\theta}^i), \quad i = 1, 2, \dots$$

Here, the parameter update $\boldsymbol{\theta}^{i+1} - \boldsymbol{\theta}^i$ is written as the solution to a linear system involving a preconditioning matrix \mathbf{P}^i and a negative energy gradient $-\mathbf{g}(\boldsymbol{\theta}^i)$. Table I shows the different preconditioners corresponding to the three optimization approaches.

Method	Preconditioner \mathbf{P}
Gradient descent	$\epsilon^{-1} \mathbf{I}$
Natural gradient descent	$\epsilon^{-1} (\mathbf{S} + \eta \mathbf{I})$
Rayleigh-Gauss-Newton	$\mathbf{H} + \epsilon^{-1} (\mathbf{S} + \eta \mathbf{I})$

TABLE I: Different preconditioners for energy minimization.

To help quantify the efficiency of these optimization approaches, Proposition 2 considers a general sequence of preconditioners $\mathbf{P}^1, \mathbf{P}^2, \dots$ and derives sharp bounds on the resulting energies $\mathcal{E}[\psi_{\boldsymbol{\theta}^1}], \mathcal{E}[\psi_{\boldsymbol{\theta}^2}], \dots$. Proposition 2 is based on standard optimization theory (e.g., [26]), but here we extend this theory to the complex-valued wavefunctions that are needed for VMC analysis.

Proposition 2. *Consider a sequence of updates $\mathbf{P}^i(\boldsymbol{\theta}^{i+1} - \boldsymbol{\theta}^i) = -\mathbf{g}(\boldsymbol{\theta}^i)$, where the inverse preconditioners $(\mathbf{P}^1)^{-1}, (\mathbf{P}^2)^{-1}, \dots$ are uniformly bounded. Suppose the parameters $\boldsymbol{\theta}^1, \boldsymbol{\theta}^2, \dots$ converge to a local energy minimizer $\boldsymbol{\theta}^*$ and the Hessian or Wirtinger Hessian is positive definite at $\boldsymbol{\theta}^*$. Then, the energies $\mathcal{E}[\psi_{\boldsymbol{\theta}^1}], \mathcal{E}[\psi_{\boldsymbol{\theta}^2}], \dots$ must satisfy*

$$\begin{aligned} \limsup_{i \rightarrow \infty} \frac{\mathcal{E}[\psi_{\boldsymbol{\theta}^{i+1}}] - \mathcal{E}[\psi_{\boldsymbol{\theta}^*}]}{\mathcal{E}[\psi_{\boldsymbol{\theta}^i}] - \mathcal{E}[\psi_{\boldsymbol{\theta}^*}]} \\ \leq \limsup_{i \rightarrow \infty} \left\| \mathbf{I} - (\mathbf{H} + \mathbf{J})^{\frac{1}{2}} \mathbf{P}_i^{-1} (\mathbf{H} + \mathbf{J})^{\frac{1}{2}} \right\|_2^2 \end{aligned}$$

or

$$\begin{aligned} \limsup_{i \rightarrow \infty} \frac{\mathcal{E}[\psi_{\boldsymbol{\theta}^{i+1}}] - \mathcal{E}[\psi_{\boldsymbol{\theta}^*}]}{\mathcal{E}[\psi_{\boldsymbol{\theta}^i}] - \mathcal{E}[\psi_{\boldsymbol{\theta}^*}]} \\ \leq \limsup_{i \rightarrow \infty} \left\| \mathbf{I} - \begin{pmatrix} \mathbf{H} & \mathbf{J} \\ \mathbf{J} & \mathbf{H} \end{pmatrix}^{\frac{1}{2}} \begin{pmatrix} \mathbf{P}_i & \mathbf{0} \\ \mathbf{0} & \overline{\mathbf{P}_i} \end{pmatrix}^{-1} \begin{pmatrix} \mathbf{H} & \mathbf{J} \\ \mathbf{J} & \mathbf{H} \end{pmatrix}^{\frac{1}{2}} \right\|_2^2 \end{aligned}$$

in the real and complex cases, respectively, where $\mathbf{H} = \mathbf{H}(\boldsymbol{\theta}^*)$ and $\mathbf{J} = \mathbf{J}(\boldsymbol{\theta}^*)$.

Proof. See Appendix A. \square

Proposition 2 ensures fast asymptotic convergence of VMC energies whenever \mathbf{J} is small and the preconditioning matrices lie close to \mathbf{H} . In particular, if the RGN method is applied with penalization parameters $\epsilon = \epsilon^i$ tending to infinity and wavefunctions $\psi_{\boldsymbol{\theta}^i}$ approaching an eigenstate of \mathcal{H} , Proposition 2 ensures the superlinear convergence

$$\limsup_{i \rightarrow \infty} \frac{\mathcal{E}[\psi_{\boldsymbol{\theta}^{i+1}}] - \mathcal{E}[\psi_{\boldsymbol{\theta}^*}]}{\mathcal{E}[\psi_{\boldsymbol{\theta}^i}] - \mathcal{E}[\psi_{\boldsymbol{\theta}^*}]} = 0.$$

In practice, our parametric class does not usually contain the *exact* ground state for \mathcal{H} , but if ϵ is large and the parametric optimizer is close to the exact ground state, then Proposition 2 still quantifies a fast linear convergence rate for RGN. In the numerical experiments presented in Section V, we achieve such a fast convergence rate by gradually moving the parameter ϵ closer to zero as we make progress in optimizing the wavefunction.

IV. VMC SAMPLING ANALYSIS

In this section, we review VMC sampling and prove a vanishing-variance principle that quantifies the sampling error in estimated energies and gradients. Then, we discuss challenges in VMC sampling and motivate several strategies to improve estimation quality.

IV.1. VMC sampling

VMC requires quantities such as \mathcal{E} , \mathbf{g} , \mathbf{S} , and \mathbf{H} that are constructed as sums or integrals over a high-dimensional or infinite-dimensional state space. To compute such quantities, VMC relies on the power of stochastic sampling. In VMC, we first generate a large number of samples $\boldsymbol{\sigma}_1, \boldsymbol{\sigma}_2, \dots, \boldsymbol{\sigma}_T$ from the normalized wavefunction density

$$\rho(\boldsymbol{\sigma}) = \frac{|\psi(\boldsymbol{\sigma})|^2}{\langle \psi, \psi \rangle}$$

using an appropriate Markov chain Monte Carlo (MCMC, [30]) sampler. Then we approximate \mathcal{E} , \mathbf{g} , \mathbf{S} , and \mathbf{H} using the following estimators:

$$\hat{\mathcal{E}} = \mathbb{E}_{\hat{\rho}}[E_{\text{loc}}(\boldsymbol{\sigma})], \quad (8)$$

$$\hat{\mathbf{g}}_i = \text{cov}_{\hat{\rho}}[\boldsymbol{\nu}_i(\boldsymbol{\sigma}), E_{\text{loc}}(\boldsymbol{\sigma})], \quad (9)$$

$$\hat{\mathbf{S}}_{ij} = \text{cov}_{\hat{\rho}}[\boldsymbol{\nu}_i(\boldsymbol{\sigma}), \boldsymbol{\nu}_j(\boldsymbol{\sigma})], \quad (10)$$

$$\begin{aligned} \hat{\mathbf{H}}_{ij} = \text{cov}_{\hat{\rho}}[\boldsymbol{\nu}_i(\boldsymbol{\sigma}), E_{\text{loc},j}(\boldsymbol{\sigma})] \\ - \hat{\mathbf{g}}_i \mathbb{E}_{\hat{\rho}}[\boldsymbol{\nu}_j(\boldsymbol{\sigma})] - \hat{\mathcal{E}} \hat{\mathbf{S}}_{ij}. \end{aligned} \quad (11)$$

Here, $\mathbb{E}_{\hat{\rho}}$ and $\text{cov}_{\hat{\rho}}$ denote expectations and covariances with respect to the empirical measure

$$\hat{\rho} = \frac{1}{T} \sum_{t=1}^T \delta_{\boldsymbol{\sigma}_t}, \quad (12)$$

and we have defined functions

$$E_{\text{loc}}(\boldsymbol{\sigma}) = \frac{\mathcal{H}\psi(\boldsymbol{\sigma})}{\psi(\boldsymbol{\sigma})}, \quad E_{\text{loc},i}(\boldsymbol{\sigma}) = \frac{\mathcal{H}\partial_{\theta_i}\psi(\boldsymbol{\sigma})}{\psi(\boldsymbol{\sigma})},$$

$$\nu_i(\boldsymbol{\sigma}) = \frac{\partial_{\theta_i}\psi(\boldsymbol{\sigma})}{\psi(\boldsymbol{\sigma})}.$$

The functions E_{loc} and ν_i are known as the local energy and logarithmic derivative, respectively.

Next we state the vanishing-variance principle, which quantifies the asymptotic variance of several VMC estimators of interest.

Proposition 3. *Assume samples $\boldsymbol{\sigma}_1, \boldsymbol{\sigma}_2, \dots, \boldsymbol{\sigma}_T$ are generated from an MCMC sampler that is geometrically ergodic with respect to the wavefunction density ρ . Assume $\mathbb{E}_\rho |E_{\text{loc}}(\boldsymbol{\sigma})|^{4+\epsilon} < \infty$ and $\sup_i \mathbb{E}_\rho |\nu_i(\boldsymbol{\sigma})|^{4+\epsilon} < \infty$ for some $\epsilon > 0$. Then, as $T \rightarrow \infty$, the errors in the estimated energies $\hat{\mathcal{E}}_T$ and gradients $\hat{\mathbf{g}}_T$ converge to Gaussian distributions as follows:*

$$\sqrt{T}(\hat{\mathcal{E}}_T - \mathcal{E}) \xrightarrow{\mathcal{D}} \mathcal{N}(0, v^2),$$

$$\sqrt{T}(\hat{\mathbf{g}}_T - \mathbf{g}) \xrightarrow{\mathcal{D}} \mathcal{N}(\mathbf{0}, \boldsymbol{\Sigma}),$$

where the asymptotic variances v^2 and $\boldsymbol{\Sigma}$ are given by

$$v^2 = \sum_{t=-\infty}^{\infty} \text{cov}[E_{\text{loc}}(\boldsymbol{\sigma}_0), E_{\text{loc}}(\boldsymbol{\sigma}_t)], \quad (13)$$

$$\boldsymbol{\Sigma}_{ij} = \sum_{t=-\infty}^{\infty} \text{cov}[\mathbf{g}'_i(\boldsymbol{\sigma}_0), \mathbf{g}'_j(\boldsymbol{\sigma}_t)], \quad (14)$$

Within (13) and (14), the covariance operator is defined with respect to the stationary process $(\boldsymbol{\sigma}_t)_{-\infty < t < \infty}$, and \mathbf{g}' is defined as

$$\mathbf{g}'(\boldsymbol{\sigma}) = \overline{(\nu(\boldsymbol{\sigma}) - \mathbb{E}_{\boldsymbol{\sigma}' \sim \rho} [\nu(\boldsymbol{\sigma}')])} (E_{\text{loc}}(\boldsymbol{\sigma}) - \mathcal{E}).$$

Proof. See Appendix A. \square

As a major takeaway from Proposition 3, if the local energy is nearly constant, i.e.,

$$E_{\text{loc}} \approx \mathcal{E}, \quad (15)$$

then the energy and energy gradients have nearly zero variance:

$$\sigma^2 \approx 0, \quad \boldsymbol{\Sigma} \approx 0.$$

This result can be viewed as a robust and quantitative extension of the classic zero-variance principle [1, 2] of VMC, which states that the energy and energy gradient estimators are perfectly accurate if the wavefunction is an eigenstate of \mathcal{H} . The vanishing-variance principle is robust, since it holds when the wavefunction is not an eigenstate, and quantitative, since it gives precise formulas for the asymptotic variances of the energy and energy gradient estimators.

IV.2. Improving estimation quality

Although the vanishing-variance principle applies to estimated gradients as well as energies, the gradients themselves converge to zero as the wavefunction approaches an eigenstate, and we glean no information about the relative accuracy. Empirical evidence suggests that noise in estimated gradients poses a major obstacle for VMC optimization, causing slow energy convergence or even spurious energy increases [11, 24]. Addressing this fundamental issue, we suggest three strategies for improving the accuracy of the estimated gradients.

The first, simplest strategy to obtain better gradient estimates is to increase the number of Monte Carlo samples. Indeed, increasing the number of samples causes a proportional decrease in the asymptotic variance of $\hat{\mathbf{g}}$, as seen in Proposition 3. To increase the number of samples, either we can run one MCMC sampler for a very long time, or equivalently we can run many MCMC samplers in parallel and then combine samples in order to evaluate \mathcal{E} , \mathbf{g} , \mathbf{S} , and \mathbf{H} . In many cases, the parallel approach leads to computational advantages, since vectorized code runs quickly and MCMC samplers can be run on multiple nodes/cores to further cut down on the runtime. For the numerical experiments reported in Section V, we run 50 MCMC samplers per CPU core across 48 CPU cores.

As a second strategy to improve gradient estimation, we can explicitly stabilize the gradient estimator. Proposition 3 reveals that the variance in $\hat{\mathbf{g}}$ depends quadratically on the deviation of the local energies E_{loc} from the mean energy \mathcal{E} . Therefore, if the MCMC sampler encounters E_{loc} values far away from \mathcal{E} , the gradient estimates can become unstable. To curb this instability, several research groups [5, 6] prefer a stabilized gradient estimator in which the most extreme local energy values are adjusted to be closer to the median. Alternatively, Luo and Clark [4] take a more extreme approach, rounding all positive gradient entries to +1, rounding all negative gradient entries to -1, and then assigning a random independent magnitude to each entry.

The shared idea in [4–6] is to mollify extreme gradient estimates, which has the benefit of improving stability but the cost of neglecting derivative information that could potentially be helpful. Therefore, we apply gradient stabilization only when needed in the numerical experiments in Section V. We calculate the Euclidean norm of each parameter update and adjust the penalization parameter ϵ as needed to ensure that the current update is not more than twice as large as the previous update. This approach, which is similar to shrinking the estimated gradient $\hat{\mathbf{g}}$, suffices to eliminate the most erratic parameter updates in our experiments.

As a third strategy for improving gradient estimates, we can optimize the MCMC sampler to minimize correlations between the samples $\boldsymbol{\sigma}_1, \boldsymbol{\sigma}_2, \dots, \boldsymbol{\sigma}_T$. Proposition 3 shows that the variance in $\hat{\mathbf{g}}$ can be very high when these time-correlations are large.

We recommend the parallel tempering method [12] as

one strategy to reduce harmful time-correlations. Parallel tempering is broadly applicable, and it has previously been applied to a variety of challenging VMC test problems [11, 31]. Parallel tempering introduces a sequence of interacting MCMC samplers, with each sampler targeting a density

$$\rho_i(\boldsymbol{\sigma}) \propto \rho(\boldsymbol{\sigma})^{i/m}, \quad i = 0, 1, \dots, m, \quad (16)$$

Periodically, the samplers targeting adjacent densities ρ_i and ρ_{i+1} swap positions, according to an appropriate Metropolis acceptance probability [32]. The chains $\rho_0, \rho_1, \dots, \rho_{m-1}$ all play a support role in the sampling; they are relatively free to traverse the configuration space unencumbered by energetic barriers, and occasionally they transmit their positions to the chain targeting ρ_m . The chain targeting ρ_m is the only chain used for estimating \mathcal{E} , \mathbf{g} , \mathbf{S} , and \mathbf{H} , and it benefits from the swap moves, which reduce time-correlations in the dynamics. We explore in more detail the benefits of parallel tempering when applied to XXZ models on large lattices in Subsection V.2.

V. NUMERICAL EXPERIMENTS

To test the performance of VMC optimization and sampling methods, we estimate ground-state energies for the transverse-field Ising (TFI) and XXZ models on 1-D and 2-D lattices with periodic boundary conditions. These models are specified by the Hamiltonians

$$\mathcal{H}_{\text{TFI}} = - \sum_{i \sim j} \sigma_i^z \sigma_j^z - h \sum_i \sigma_i^x, \quad (17)$$

$$\mathcal{H}_{\text{XXZ}} = -\Delta \sum_{i \sim j} \sigma_i^z \sigma_j^z + \sum_{i \sim j} \sigma_i^y \sigma_j^y - \sigma_i^x \sigma_j^x, \quad (18)$$

where h and Δ are real-valued parameters. The XXZ model is sometimes alternatively defined as

$$\mathcal{H}_{\text{XXZ}} = \Delta \sum_{i \sim j} \sigma_i^z \sigma_j^z + \sum_{i \sim j} \sigma_i^x \sigma_j^x + \sigma_i^y \sigma_j^y,$$

which is a unitary transformation of (18), assuming a bipartite lattice. As a consequence of the Perron-Frobenius theorem and translational symmetry, the TFI and XXZ models admit unique, translationally symmetric ground-state wavefunctions. For 1-D lattices but not 2-D lattices, exact ground-state wavefunctions are also known [33, 34].

As a wavefunction ansatz, we use a restricted Boltzmann machine (RBM), which can be written as

$$\psi_{\mathbf{w}, \mathbf{b}}(\boldsymbol{\sigma}) = \prod_{i=1}^{\alpha} \prod_{\mathcal{T}} \cosh \left(\sum_j \mathbf{w}_{ij} (\mathcal{T} \boldsymbol{\sigma})_j + \mathbf{b}_i \right).$$

Here, \mathcal{T} ranges over the translation operators on the periodic lattice, and \mathbf{w} and \mathbf{b} are vectors of complex-valued parameters, called *weights* and *biases*. This ansatz is an example of a two-layer neural network and is a simplification of the RBM ansatz used for VMC optimization in

[3]. The ansatz involves $\alpha(n+1)$ parameters, where n is the number of spins and we set $\alpha = 5$ for all of our numerical experiments. We report additional implementation details in Appendix B.

V.1. Comparing optimization methods

To compare different VMC optimizers in the noiseless setting, we consider the TFI model on a 10×1 lattice, which is small enough so that \mathcal{E} , \mathbf{g} , \mathbf{S} , and \mathbf{H} can be computed by exact summation, avoiding the need for stochastic sampling. In Figure 2, we present the energy error profiles of GD, natural GD, and RGN in this setting, i.e., with deterministic parameter updates. We find that RGN leads to faster energy convergence and reduced energy errors compared to GD and natural GD. RGN achieves very low energy errors ($< 10^{-7}$) after just 100–150 iterations, whereas natural GD requires more than 1000 iterations to achieve such high accuracies.

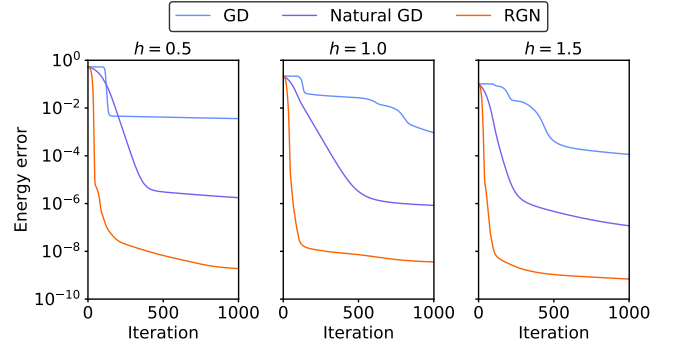


FIG. 2. RGN achieves low energy errors in ferromagnetic ($h = 0.5$, left), transitional ($h = 1.0$, center), and paramagnetic ($h = 1.5$, right) regimes. Plot shows relative error in ground-state energy estimates.

In light of Proposition 2, we expect the most rapid energy convergence when the preconditioner is close to the true Hessian ($\frac{\mathbf{H}}{\mathbf{J}} \frac{\mathbf{J}}{\mathbf{H}}$). Indeed, in Figure 3, we confirm that the Hessian approximation used in RGN closely approximates the true Hessian, in concordance with the fast observed convergence rate.

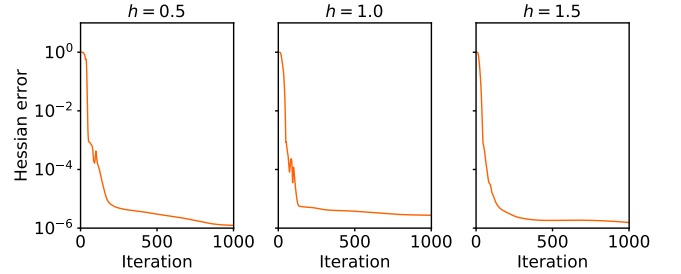


FIG. 3. RGN achieves accurate Hessian approximations with relative errors $< 10^{-5}$ for most iterations. Plot shows relative error $|\left(\frac{\mathbf{g}}{\mathbf{J}}\right)| / \left|\left(\frac{\mathbf{H}}{\mathbf{J}}\right)\right|$ computed at each iteration.

V.2. Challenges in VMC sampling

We next extend VMC to larger lattices by using MCMC sampling. For the TFI model, we initialize our MCMC samplers from configurations chosen uniformly at random and propose random updates based on flipping a single spin. We then accept or reject these updates according to an appropriate Metropolis acceptance probability [32]. In contrast, for the XXZ model, we confine our MCMC samplers to ‘balanced’ configurations for which the magnetization is the same on both components of the bipartite lattice, since the ground-state wavefunction is only supported on these configurations. We initialize from random balanced configurations and propose random balanced updates based on flipping two spins. We run our MCMC samplers for $20 \times n$ time steps per iteration and calculate the local energies and logarithmic derivatives once every n time steps, where n denotes the number of spins.

Our MCMC samplers are guaranteed to decorrelate quickly when sampling the ground-state wavefunctions for the TFI model at $h = \infty$ or the XXZ model at $\Delta = -1$. For these extreme parameter settings, every Metropolis proposal is accepted, the relaxation time for the TFI sampler is $n/2$ [35], and the relaxation time for the XXZ sampler is $n/4$ [36]. Yet there is no guarantee that our MCMC samplers remain efficient for the models and parametrized wavefunctions more reasonably encountered.

Indeed, the RGN optimizer encounters difficulties when calculating ground-state energies for the XXZ model, as shown in Figure 4. During the first 100–200 iterations, the RGN energies decrease quickly. However, at iteration 190 ($\Delta = 1.5$) or 270 ($\Delta = 1.0$), we observe a large energy spike, which persists over hundreds of optimization steps. The energy spike occurs because the wavefunction has experienced overfitting, achieving a highly optimized structure over a large class of spin configurations but a poorly optimized structure (high densities, high local energies) in far-away configurations that have not been sampled yet. When the MCMC samplers eventually visit the poorly optimized configurations, they become stuck due to the high densities, the energy estimates spike, and the optimizer begins the slow process of repairing the wavefunction. In contrast, because natural GD optimizes the wavefunction more gradually, it is apparently less sensitive to overfitting.

To improve the sampling for the XXZ model with $\Delta = 1.0$ and $\Delta = 1.5$, we apply the parallel tempering method described in Section IV.2 using fifty target densities. Although parallel tempering does not completely eliminate the energy spikes, it reduces their magnitudes and leads to quicker restoration cycles, as shown in Figure 5. Using parallel tempering, we find after 500 iterations that RGN energy estimates are typically an order of magnitude more accurate than the energy estimates from natural GD.

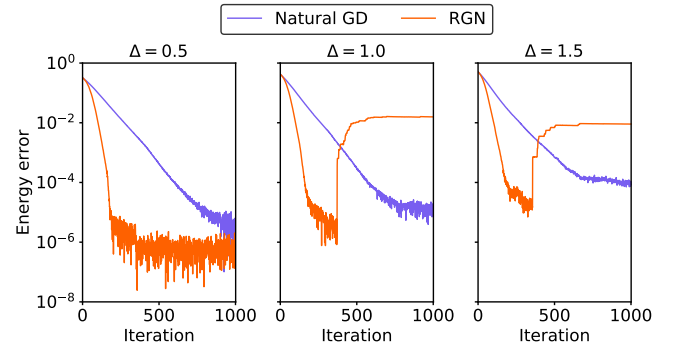


FIG. 4. RGN can lead to energy spikes if direct MCMC sampling is used. Plot shows relative error in ground-state energy estimates for an XXZ model on a 100×1 lattice.

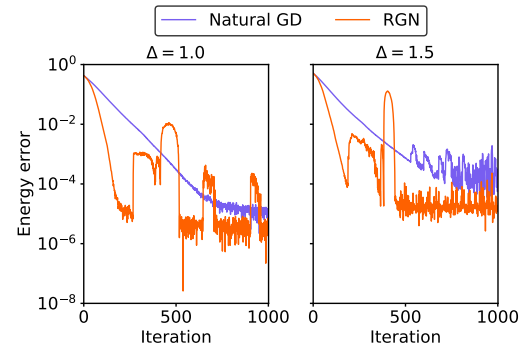


FIG. 5. RGN is able to recover from energy spikes if parallel tempering is used. Natural GD shows small energy spikes as well as RGN in the $\Delta = 1.5$ case (right panel).

V.3. Results for larger systems

In this final subsection, we report the accuracy of estimated ground-state energies for TFI and XXZ models on lattices with up to 400 spins. These are some of the largest spin systems ever treated using VMC (the current record is 441 spins [8, 10]). However, we are able to train highly accurate VMC wavefunctions for these large lattices by using RGN and (for some XXZ models) parallel tempering. We compare the estimated ground-state energies against exact ground-state energies, when available, in Table II. We report the estimated energies themselves in Table III if exact ground-state energies are unavailable.

Summarizing Tables II and III, we find that RGN compares favorably to the natural GD approach previously used in [3] to obtain benchmark variational estimates for ground-state TFI and XXZ wavefunctions. In 1-D lattices, RGN reduces natural GD energy errors by up to four orders of magnitude, reaching error levels as low as 1.0×10^{-9} and 1.6×10^{-9} . In 2-D lattices for which exact reference energies are not available, the energy estimates obtained by RGN are typically lower than those obtained using natural GD and have reduced variance.

We further illustrate the comparison between natural

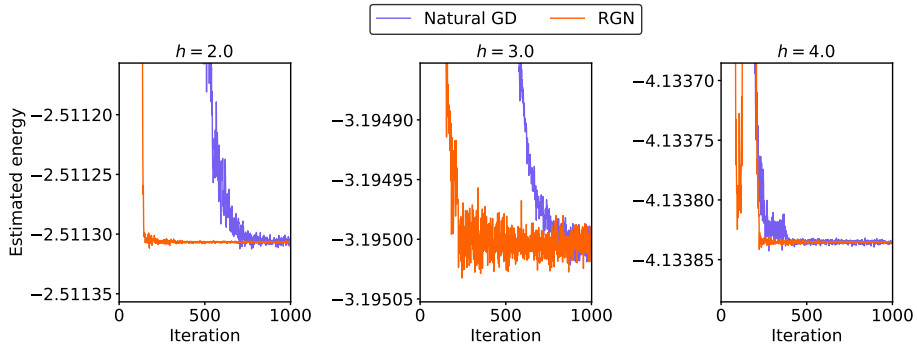


FIG. 6. RGN outperforms natural GD in ferromagnetic ($h = 0.5$, left), transitional ($h = 1.0$, center), and paramagnetic ($h = 1.5$, right) Ising models on a 20×20 lattice. Plot shows ground-state energy estimates normalized by the number of sites.

200 \times 1 TFI model			
	$h = 0.5$	$h = 1.0$	$h = 1.5$
Natural GD	3.9×10^{-5}	1.4×10^{-4}	8.5×10^{-8}
RGN	1.0×10^{-9}	2.9×10^{-6}	1.6×10^{-9}
100 \times 1 XXZ model			
	$\Delta = 0.5$	$\Delta = 1.0$	$\Delta = 1.5$
Natural GD	3.9×10^{-6}	1.2×10^{-5}	5.4×10^{-5}
RGN	2.5×10^{-7}	3.3×10^{-6}	2.0×10^{-5}

TABLE II: Relative errors in ground-state energy estimates.

20 \times 20 TFI model			
	$h = 2.0$	$h = 3.0$	$h = 4.0$
Natural GD	-2.5113061	-3.195003	-4.1338352
	± 0.0000023	± 0.000008	± 0.0000011
RGN	-2.5113069	-3.195000	-4.1338354
	± 0.0000005	± 0.000010	± 0.0000002

TABLE III: Ground-state energy estimates $\pm 1\sigma$ errors, normalized by the number of sites.

GD and RGN in Figures 6 and 7. These figures, showing the complete time series of energy estimates over 1000 optimization steps, reveal that RGN results after 200 iterations are typically more accurate for TFI models than natural GD results after 1000 iterations. Because RGN is only slightly more expensive than natural GD (less than a factor of two in our experiments), we conclude that RGN makes it possible to obtain accurate ground state estimates with reduced training time and overall computational cost.

VI. CONCLUSION

This work has presented both theoretical and computational contributions to improving ground-state energy estimates in VMC. First, we showed that the energy Hessian simplifies dramatically near an eigenstate, depend-

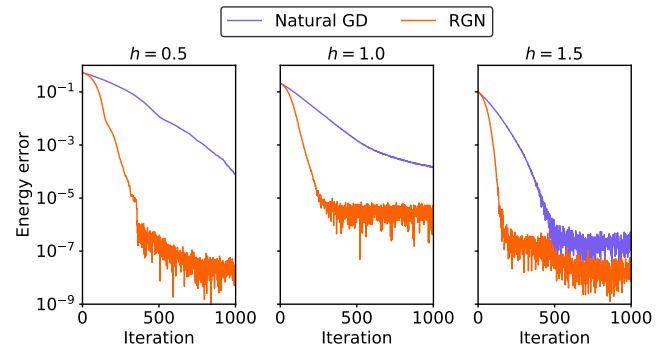


FIG. 7. Relative error in ground-state energy estimates for TFI models on a 200×1 lattice.

ing only on first derivatives of the wavefunction with respect to the parameters. Taking advantage of this simplification, we introduced a new Rayleigh-Gauss-Newton (RGN) optimizer that can achieve superlinear convergence. Second, we proved a vanishing-variance property that guarantees VMC energy estimates exhibit reduced variance near an eigenstate. This principle ensures relative accuracy in the energies but not the gradients, so we suggested a parallel tempering approach to improve gradient estimation for challenging test problems.

We highlight two opportunities for improving our optimization and sampling methods even further. First, for very large parametrizations, the linear system solve in the RGN method becomes numerically challenging. To address this difficulty, the KFAC method for efficient matrix inversion within natural gradient descent [5, 37], in addition to the aforementioned matrix-free approach [28], could potentially be adapted to RGN. Second, while parallel tempering is a simple, broadly applicable enhanced sampling method, there exists a variety of alternative methods [38]. We anticipate that further analysis of and experimentation with enhanced MCMC sampling will play an important role in realizing the full potential of VMC in future applications.

ACKNOWLEDGMENTS

RJW and ML would like to acknowledge helpful conversations with Timothy Berkelbach, Aaron Dinner, Sam Greene, Lin Lin, Verena Neufeld, James Smith, Jonathan Siegel, Erik Thiede, Jonathan Weare, and Huan Zhang. RJW is supported by New York University's Dean's Dissertation Fellowship and by the National Science Foundation through award DMS-1646339. ML is supported by the National Science Foundation under Award No. 1903031. Computing resources were provided by New York University's High Performance Computing.

Appendix A: Proofs

Proof of Proposition 2. We prove only the second result. The first result is well-known, and the proof is similar. Because the wavefunction is analytic at $\boldsymbol{\theta}^*$ and the Wirtinger Hessian $(\frac{\mathbf{H}}{\mathbf{J}} \frac{\mathbf{J}}{\mathbf{H}})$ is positive definite, as $i \rightarrow \infty$ we find

$$\left(\frac{\mathbf{g}(\boldsymbol{\theta}^i)}{\mathbf{g}(\boldsymbol{\theta}^i)} \right) \sim \left(\frac{\mathbf{H}}{\mathbf{J}} \frac{\mathbf{J}}{\mathbf{H}} \right) \left(\frac{\boldsymbol{\theta}^i - \boldsymbol{\theta}^*}{\boldsymbol{\theta}^i - \boldsymbol{\theta}^*} \right).$$

and

$$\mathcal{E}[\psi_{\boldsymbol{\theta}^i}] - \mathcal{E}[\psi_{\boldsymbol{\theta}^*}] \sim \frac{1}{2} \left| \left(\frac{\mathbf{H}}{\mathbf{J}} \frac{\mathbf{J}}{\mathbf{H}} \right)^{\frac{1}{2}} \left(\frac{\boldsymbol{\theta}^i - \boldsymbol{\theta}^*}{\boldsymbol{\theta}^i - \boldsymbol{\theta}^*} \right) \right|^2$$

Hence, the i -th parameter update satisfies

$$\begin{aligned} & \left(\frac{\boldsymbol{\theta}^{i+1} - \boldsymbol{\theta}^*}{\boldsymbol{\theta}^{i+1} - \boldsymbol{\theta}^*} \right) \\ & \sim \left[\mathbf{I} - \left(\begin{array}{cc} \mathbf{P}^i & \mathbf{0} \\ \mathbf{0} & \mathbf{P}^i \end{array} \right)^{-1} \left(\frac{\mathbf{H}}{\mathbf{J}} \frac{\mathbf{J}}{\mathbf{H}} \right) \right] \left(\boldsymbol{\theta}^i - \boldsymbol{\theta}^* \overline{\boldsymbol{\theta}^i - \boldsymbol{\theta}^*} \right) \\ & \quad + \mathcal{O}(|\boldsymbol{\theta} - \boldsymbol{\theta}^*|^2). \end{aligned}$$

Moreover, the energy ratio satisfies

$$\frac{\mathcal{E}[\psi_{\boldsymbol{\theta}^{i+1}}] - \mathcal{E}[\psi_{\boldsymbol{\theta}^*}]}{\mathcal{E}[\psi_{\boldsymbol{\theta}^i}] - \mathcal{E}[\psi_{\boldsymbol{\theta}^*}]} \sim \frac{\left| \left[\mathbf{I} - \left(\frac{\mathbf{H}}{\mathbf{J}} \frac{\mathbf{J}}{\mathbf{H}} \right)^{\frac{1}{2}} \left(\begin{array}{cc} \mathbf{P}^i & \mathbf{0} \\ \mathbf{0} & \mathbf{P}^i \end{array} \right)^{-1} \left(\frac{\mathbf{H}}{\mathbf{J}} \frac{\mathbf{J}}{\mathbf{H}} \right)^{\frac{1}{2}} \right] \left(\frac{\mathbf{H}}{\mathbf{J}} \frac{\mathbf{J}}{\mathbf{H}} \right)^{\frac{1}{2}} \left(\frac{\boldsymbol{\theta}_i - \boldsymbol{\theta}^*}{\boldsymbol{\theta}^i - \boldsymbol{\theta}^*} \right) \right|^2}{\left| \left(\frac{\mathbf{H}}{\mathbf{J}} \frac{\mathbf{J}}{\mathbf{H}} \right)^{\frac{1}{2}} \left(\frac{\boldsymbol{\theta}_i - \boldsymbol{\theta}^*}{\boldsymbol{\theta}^i - \boldsymbol{\theta}^*} \right) \right|^2},$$

whence

$$\begin{aligned} & \limsup_{i \rightarrow \infty} \frac{\mathcal{E}[\psi_{\boldsymbol{\theta}^{i+1}}] - \mathcal{E}[\psi_{\boldsymbol{\theta}^*}]}{\mathcal{E}[\psi_{\boldsymbol{\theta}^i}] - \mathcal{E}[\psi_{\boldsymbol{\theta}^*}]} \\ & \leq \left\| \mathbf{I} - \left(\frac{\mathbf{H}}{\mathbf{J}} \frac{\mathbf{J}}{\mathbf{H}} \right)^{\frac{1}{2}} \left(\begin{array}{cc} \mathbf{P}_i & \mathbf{0} \\ \mathbf{0} & \mathbf{P}_i \end{array} \right)^{-1} \left(\frac{\mathbf{H}}{\mathbf{J}} \frac{\mathbf{J}}{\mathbf{H}} \right)^{\frac{1}{2}} \right\|_2^2. \end{aligned}$$

□

Proof of Proposition 3. The Markov chain central limit theorem [39] guarantees that

$$\frac{1}{T} \sum_{t=1}^T \left(\begin{array}{c} \overline{\boldsymbol{\nu}(\boldsymbol{\sigma}_t)} \\ E_{\text{loc}}(\boldsymbol{\sigma}_t) \end{array} \right) = \left(\begin{array}{c} \mathbb{E}_\rho[\overline{\boldsymbol{\nu}(\boldsymbol{\sigma})}] \\ \mathcal{E} \end{array} \right) + \mathcal{O}_P\left(\frac{1}{\sqrt{T}}\right)$$

as $T \rightarrow \infty$. Next, using the identity

$$\begin{aligned} & (\mathbf{x} - \mathbb{E}_\rho[\overline{\boldsymbol{\nu}(\boldsymbol{\sigma})}]) (y - \mathcal{E}) \\ & = \mathcal{O}(|\mathbf{x} - \mathbb{E}_\rho[\overline{\boldsymbol{\nu}(\boldsymbol{\sigma})}]|^2 + |y - \mathcal{E}|^2) \end{aligned}$$

and substituting the empirical averages $\mathbf{x} =$

$\frac{1}{T} \sum_{t=1}^T \overline{\boldsymbol{\nu}(\boldsymbol{\sigma}_t)}$ and $y = \frac{1}{T} \sum_{t=1}^T E_{\text{loc}}(\boldsymbol{\sigma}_t)$, we obtain

$$\begin{aligned} & \hat{\mathbf{g}}_T \\ & = \frac{1}{T} \sum_{t=1}^T \overline{\boldsymbol{\nu}(\boldsymbol{\sigma}_t)} E_{\text{loc}}(\boldsymbol{\sigma}_t) - \frac{1}{T} \sum_{t=1}^T \overline{\boldsymbol{\nu}(\boldsymbol{\sigma}_t)} \frac{1}{T} \sum_{t=1}^T E_{\text{loc}}(\boldsymbol{\sigma}_t) \\ & = \frac{1}{T} \sum_{t=1}^T (\overline{\boldsymbol{\nu}(\boldsymbol{\sigma}_t)} - \mathbb{E}_\rho[\overline{\boldsymbol{\nu}(\boldsymbol{\sigma})}]) (E_{\text{loc}}(\boldsymbol{\sigma}_t) - \mathcal{E}) + \mathcal{O}_P\left(\frac{1}{T}\right) \\ & = \frac{1}{T} \sum_{t=1}^T \mathbf{g}'(\boldsymbol{\sigma}_t) + \mathcal{O}_P\left(\frac{1}{T}\right). \end{aligned}$$

Slutsky's lemma shows that the $\mathcal{O}_P\left(\frac{1}{T}\right)$ term is asymptotically negligible, and another application of the Markov chain central limit theorem guarantees

$$\begin{aligned} & \sqrt{T}(\hat{\mathcal{E}}_T - \mathcal{E}) \xrightarrow{\mathcal{D}} \mathcal{N}(0, v^2), \\ & \sqrt{T}(\hat{\mathbf{g}}_T - \mathbf{g}) \xrightarrow{\mathcal{D}} \mathcal{N}(\mathbf{0}, \boldsymbol{\Sigma}), \end{aligned}$$

where the asymptotic variances v^2 and $\boldsymbol{\Sigma}$ are as given in (13) and (14). □

Appendix B: Computations

Here, we discuss the computational details for our experiments. These computations are implemented using the JAX library for Python [40], and complete scripts and output are available on github [41]. Using these scripts, estimating the ground-state wavefunction for a large lattice is relatively fast, requiring less than four days on a single 48-core CPU node.

For 1-D and 2-D lattices, we can evaluate the log wavefunction and its derivatives in $\mathcal{O}(\alpha n \log n)$ operations using the discrete Fourier transform \mathcal{F} and its inverse \mathcal{F}^{-1} . To show this, we write

$$\log \psi_{\mathbf{w}, \mathbf{b}}(\boldsymbol{\sigma}) = \sum_{i=1}^{\alpha} \sum_j \log \cosh \boldsymbol{\theta}_{ij},$$

where we have introduced angles

$$\boldsymbol{\theta}_{ij} = (\mathcal{F}^{-1} (\mathcal{F} \mathbf{w}_i \odot \mathcal{F} \boldsymbol{\sigma}))_j + \mathbf{b}_i$$

and we have used \odot to represent element-wise multiplication. Similarly, we write

$$\begin{aligned} \frac{\partial \log \psi_{\mathbf{w}, \mathbf{b}}}{\partial \mathbf{b}_i}(\boldsymbol{\sigma}) &= \sum_j \tanh \boldsymbol{\theta}_{ij}, \\ \frac{\partial \log \psi_{\mathbf{w}, \mathbf{b}}}{\partial \mathbf{w}_{ij}}(\boldsymbol{\sigma}) &= (\mathcal{F}^{-1} (\mathcal{F} (\tanh \boldsymbol{\theta}_{i \cdot}) \odot \mathcal{F} \boldsymbol{\sigma}))_j. \end{aligned}$$

Before evaluating the wavefunction $\psi(\boldsymbol{\sigma})$ or wavefunction derivative $\psi_i(\boldsymbol{\sigma})$, we check whether $\boldsymbol{\sigma}$ has ‘mostly negative’ magnetization, as defined by

$$2 \sum_i \boldsymbol{\sigma}_i + \boldsymbol{\sigma}_1 < 0. \quad (\text{B1})$$

If we encounter a configuration $\boldsymbol{\sigma}$ for which (B1) is not satisfied, we transform it to $-\boldsymbol{\sigma}$. Indeed, the mostly

negative configurations suffice to determine the complete wavefunction given the symmetry condition $\psi(\boldsymbol{\sigma}) = \psi(-\boldsymbol{\sigma})$, and VMC can lead to low-quality ground-state wavefunction estimates when this symmetry condition is not enforced.

We initialize our neural network wavefunction parameters as independent complex-valued $\mathcal{N}(0, 0.001)$ random variables, using a random seed of 123. We then update our parameters using GD, natural GD, or RGN over 1000 iterations, as described in Algorithms 1 and 2. During the optimizations, we increase the penalization parameter ϵ from $\epsilon = \epsilon_{\min}$ to $\epsilon = \epsilon_{\max}$ and increase η from $\eta = \eta_{\min}$ to $\eta = \eta_{\max}$ at a geometric rate over τ iterations. Our specific choices of parameters ϵ_{\min} , ϵ_{\max} , η_{\min} , η_{\max} , and τ are detailed below in Table IV.

ϵ_{\min}	0.001
ϵ_{\max}	0.01 for GD and natural GD, 1000 for RGN
η_{\min}	0.001
η_{\max}	0.001 for natural GD, 0.1 for RGN
τ	100 for deterministic updates, 500 for stochastic updates

TABLE IV: Penalization parameters

When optimizing VMC wavefunctions, we occasionally encounter a sudden increase in the norm of the parameter updates, here defined as a factor of two or greater. When such a large update occurs, in addition to immediately restricting the size of the parameter update (by decreasing ϵ), we restore $\epsilon = \epsilon_{\min}$ and $\eta = \eta_{\min}$ and restart the geometric progression.

Lastly, after completing our optimizations, we run the MCMC chains for an additional $2000 \times n$ time steps and calculate local energies once per every n time steps to obtain the energy estimates reported in Tables II and III.

[1] J. Gubernatis, N. Kawashima, and P. Werner, *Quantum Monte Carlo Methods* (Cambridge University Press, 2016).

[2] F. Becca and S. Sorella, *Quantum Monte Carlo Approaches for Correlated Systems* (Cambridge University Press, 2017).

[3] G. Carleo and M. Troyer, Solving the quantum many-body problem with artificial neural networks, *Science* **355**, 602 (2017).

[4] D. Luo and B. K. Clark, Backflow transformations via neural networks for quantum many-body wave functions, *Physical Review Letters* **122**, 226401 (2019).

[5] D. Pfau, J. S. Spencer, A. G. Matthews, and W. M. C. Foulkes, Ab initio solution of the many-electron Schrödinger equation with deep neural networks, *Physical Review Research* **2**, 033429 (2020).

[6] J. Hermann, Z. Schätzle, and F. Noé, Deep-neural-network solution of the electronic Schrödinger equation, *Nature Chemistry* , 1 (2020).

[7] J. S. Spencer, D. Pfau, A. Botev, and W. M. C. Foulkes, Better, faster fermionic neural networks, arXiv preprint arXiv:2011.07125 (2020).

[8] O. Sharir, Y. Levine, N. Wies, G. Carleo, and A. Shashua, Deep autoregressive models for the efficient variational simulation of many-body quantum systems, *Physical Review Letters* **124**, 020503 (2020).

[9] L. Yang, Z. Leng, G. Yu, A. Patel, W.-J. Hu, and H. Pu, Deep learning-enhanced variational Monte Carlo method for quantum many-body physics, *Physical Review Research* **2**, 012039 (2020).

[10] L. Yang, W. Hu, and L. Li, Scalable variational Monte Carlo with graph neural ansatz, arXiv preprint arXiv:2011.12453 (2020).

[11] C.-Y. Park and M. J. Kastoryano, Geometry of learning neural quantum states, *Physical Review Research* **2**, 023232 (2020).

- [12] R. H. Swendsen and J.-S. Wang, Replica Monte Carlo simulation of spin-glasses, *Physical Review Letters* **57**, 2607 (1986).
- [13] S. Sachdev, *Quantum Phase Transitions* (Cambridge University Press, 2009).
- [14] J. G. Ángyán and P. R. Surján, Normalization corrections to perturbation theory for the time-independent nonlinear Schrödinger equation, *Physical Review A* **44**, 2188 (1991).
- [15] W. Wirtinger, Zur formalen theorie der funktionen von mehr komplexen veränderlichen, *Mathematische Annalen* **97**, 357 (1927).
- [16] P. J. Schreier and L. L. Scharf, Complex differential calculus (Wirtinger calculus), in *Statistical Signal Processing of Complex-Valued Data: The Theory of Improper and Noncircular Signals* (Cambridge University Press, 2010) pp. 277–286.
- [17] S. Sorella, Generalized Lanczos algorithm for variational quantum Monte Carlo, *Physical Review B* **64**, 024512 (2001).
- [18] S. Sorella, M. Casula, and D. Rocca, Weak binding between two aromatic rings: Feeling the van der Waals attraction by quantum Monte Carlo methods, *The Journal of Chemical Physics* **127**, 014105 (2007).
- [19] J. Stokes, J. Izaac, N. Killoran, and G. Carleo, Quantum natural gradient, *Quantum* **4**, 269 (2020).
- [20] D. P. Kingma and J. Ba, Adam: A method for stochastic optimization, in *3rd International Conference on Learning Representations, ICLR 2015, San Diego, CA, USA, May 7-9, 2015, Conference Track Proceedings*, edited by Y. Bengio and Y. LeCun (2015).
- [21] S. J. Reddi, S. Kale, and S. Kumar, On the convergence of Adam and beyond, in *International Conference on Learning Representations* (2018).
- [22] I. Sabzevari, A. Mahajan, and S. Sharma, An accelerated linear method for optimizing non-linear wavefunctions in variational Monte Carlo, *The Journal of Chemical Physics* **152**, 024111 (2020).
- [23] M. Hibat-Allah, M. Ganahl, L. E. Hayward, R. G. Melko, and J. Carrasquilla, Recurrent neural network wave functions, *Physical Review Research* **2**, 023358 (2020).
- [24] T. Westerhout, N. Astrakhantsev, K. S. Tikhonov, M. I. Katsnelson, and A. A. Bagrov, Generalization properties of neural network approximations to frustrated magnet ground states, *Nature Communications* **11**, 1 (2020).
- [25] D. Wierichs, C. Gogolin, and M. Kastoryano, Avoiding local minima in variational quantum eigensolvers with the natural gradient optimizer, *Physical Review Research* **2**, 043246 (2020).
- [26] J. Nocedal and S. Wright, *Numerical Optimization* (Springer Science & Business Media, 2006).
- [27] A. Cuzzocrea, A. Scemama, W. J. Briels, S. Moroni, and C. Filippi, Variational principles in quantum Monte Carlo: The troubled story of variance minimization, *Journal of Chemical Theory and Computation* **16**, 4203 (2020).
- [28] E. Neuscamman, C. Umrigar, and G. K.-L. Chan, Optimizing large parameter sets in variational quantum Monte Carlo, *Physical Review B* **85**, 045103 (2012).
- [29] L. Zhao and E. Neuscamman, A blocked linear method for optimizing large parameter sets in variational Monte Carlo, *Journal of Chemical Theory and Computation* **13**, 2604 (2017).
- [30] J. S. Liu, *Monte Carlo Strategies in Scientific Computing* (Springer Science & Business Media, 2008).
- [31] K. Choo, G. Carleo, N. Regnault, and T. Neupert, Symmetries and many-body excitations with neural-network quantum states, *Physical Review Letters* **121**, 167204 (2018).
- [32] N. Metropolis, A. W. Rosenbluth, M. N. Rosenbluth, A. H. Teller, and E. Teller, Equation of state calculations by fast computing machines, *The Journal of Chemical Physics* **21**, 1087 (1953).
- [33] H. Bethe, Zur theorie der metalle, *Zeitschrift für Physik* **71**, 205 (1931).
- [34] P. Pfeuty, The one-dimensional Ising model with a transverse field, *Annals of Physics* **57**, 79 (1970).
- [35] D. A. Levin and Y. Peres, *Markov Chains and Mixing Times*, Vol. 107 (American Mathematical Soc., 2017).
- [36] P. Diaconis, *Group Representations in Probability and Statistics*, Institute of Mathematical Statistics Lecture Notes—Monograph Series, 11 (Institute of Mathematical Statistics, Hayward, CA, 1988).
- [37] J. Martens and R. Grosse, Optimizing neural networks with Kronecker-factored approximate curvature, in *Proceedings of the 32nd International Conference on International Conference on Machine* (2015).
- [38] P. Tiwary and A. van de Walle, A review of enhanced sampling approaches for accelerated molecular dynamics, *Multiscale Materials Modeling for Nanomechanics* , 195 (2016).
- [39] G. L. Jones *et al.*, On the Markov chain central limit theorem, *Probability Surveys* **1**, 299 (2004).
- [40] J. Bradbury, R. Frostig, P. Hawkins, M. J. Johnson, C. Leary, D. Maclaurin, G. Necula, A. Paszke, J. Vander-Plas, S. Wanderman-Milne, and Q. Zhang, JAX: Composable transformations of Python+NumPy programs (2018).
- [41] R. J. Webber, RGN optimization, https://github.com/rjwebber/rgn_optimization (2021).